

Experimental time-lapse visualization of mud-filtrate invasion and mudcake deposition in complex rocks using X-ray radiography

Pierre Aéréns^{1,*}, Carlos Torres-Verdín¹, and Nicolas Espinoza¹

¹The University of Texas at Austin

Abstract. Accurate description and modeling of multiphase fluid flow is of paramount importance for subsurface resource engineering. The main source of information to quantify *in situ* rock properties are borehole geophysical measurements, which are very often riddled with uncertainty ensuing from both rock heterogeneity/anisotropy and mud-filtrate invasion effects. Therefore, experimental methods are needed to accurately describe and quantify the physics of mud-filtrate invasion and mudcake deposition and its effects on borehole geophysical measurements. We develop a new high-resolution experimental method to investigate the invasion of water- and oil-base drilling muds into air-, brine- or oil-saturated rock samples using X-ray radiography. During mud injection, rock samples are scanned using high-resolution X-ray radiography, enabling the time-lapse visualization of both mud-filtrate invasion and external/internal mudcake deposition. Our experimental method successfully examines the effects of rock heterogeneity, bedding plane orientation, and anisotropy on the spatial distribution of fluids and mudcake formation resulting from mud-filtrate invasion. It also emphasizes the importance of initial fluid saturations and mud properties on the final fluid saturation state once mudcake seals the borehole. The procedure is fast, accurate, and reliable to quantify the process of mud-filtrate invasion at the core scale, enabling improved understanding of invasion effects on borehole geophysical measurements following drilling operations, especially in spatially complex rocks such as laminated sandstones and carbonates.

1 Introduction

Spatially heterogeneous reservoirs continue to be challenging for subsurface energy specialists. Appraisal of petroleum reservoirs and quantification of reserves rely heavily on borehole geophysical measurements, which remain the main source of data from the subsurface. However, borehole geophysical measurements are known to be greatly affected by uncertainty arising from rock heterogeneity and mud-filtrate invasion effects. It is therefore extremely important to properly understand and characterize the physical processes governing mud-filtrate invasion and mudcake deposition, in order to correct for their effects and accurately interpret borehole measurements, especially in heterolithic rocks. Description of multiphase flow in highly heterogeneous rocks during drilling operations requires experimental and numerical methods that integrate all information available on rock formations, *in situ* or drilling fluids, and their interactions. Given that it cannot be measured directly, numerical methods have been developed to estimate the radius of mud-filtrate invasion, from borehole measurements [1]. Unfortunately, these numerical methods remain subject to uncertainty and require comprehensive understanding of the physics of invasion and mudcake deposition, which can only be attained from experimental results.

Mud-filtrate invasion has been the focus of experimental research since the 1930s; numerous researchers have since expanded the scope of this research to include more and more complex cases and mechanisms [2, 3]. However, most of the available technical literature on the subject remains limited to

homogeneous rocks and/or unrealistic rock properties or configurations. At the same time, recent experimental procedures introduced industrial CT scanners to examine more realistic rock and borehole conditions during invasion, and to quantify *in situ* mud-filtrate invasion and mudcake deposition using X-ray computed tomography (CT) [4]. Historically, *in situ* visualization of fluids or flow inside opaque structures, such as rock samples, has been technically challenging. Over time, several methods have been explored and tested to determine *in situ* fluid distributions during coreflooding, including the use of transparent models, electrical resistivity, or nuclear magnetic resonance measurements, with each of these techniques presenting limitations [5]. Nevertheless, none of these methods rival X-ray CT when it comes to providing a fast and accurate measurement of fluid saturations or their spatial distribution. X-ray CT is a powerful tool with a vast range of applications that enables the non-destructive visualization of internal structures within objects. A CT scanner generates detailed three-dimensional (3D) images by relying on the difference in X-ray absorption resulting from the difference in atomic structure (density) of different materials present in the sample. CT imaging in the geosciences has gained considerable attention over the last decades, with modified medical X-ray CT scanners being an integral part of core analysis laboratories around the world. A more recent addition to the list of available tools was the introduction of industrial microfocus X-ray CT scanners, referred to as microCT scanners. Industrial microCT scanners rely on the same physical phenomenon to generate 3D images similar to

* Corresponding author: pierre.aerens@utexas.edu

those delivered by medical CT scanners. However, contrary to medical CT scanners that rotate the X-ray source and detector around the (typically) live specimen being scanned, microCT scanners are built such that the X-ray source (called the X-ray gun) and the detector are fixed, while the sample is placed on a rotating stage. Moreover, microCT scanners can be used at higher powers, hence at greater spatial resolution, because they are not bound by radiation limits [6, 7, 8].

We describe a new experimental procedure to monitor and study mud-filtrate invasion and mudcake deposition under conditions that resemble those typically encountered in a borehole. The experimental system is composed of an X-ray microCT scanner and an automated injection pump, enabling mud injection to take place inside the shielded cabinet of the microCT scanner. Instead of using a traditional cylindrical geometry, rectangular slabs are used to monitor the process of invasion [9]; slab dimensions are such that they can be assumed two-dimensional (2D) because fluid transport within the sample can be considered negligible in the direction perpendicular to its main plane, making the invasion front homogeneous in this direction too. Such a condition makes 2D X-ray radiography viable to monitor the experiment and eliminates the need for micro-computed tomography and data reconstruction. Mud-filtrate invasion takes place when drilling mud is forced into the diffuser at the inlet of the custom-made flow cell while the outlet is vented to atmospheric pressure. During mud injection, the rock core sample is scanned quasi-continuously using high-resolution X-ray radiography to capture and quantify both mud-filtrate invasion and mudcake deposition as a function of time.

2 Materials and methods

This section describes (1) the physics of X-ray CT as well as the imaging technique used during mud injection, (2) the experimental procedure, and finally (3) how the X-ray radiographs were processed to visualize mud-filtrate invasion.

As described above, a microCT scanner produces a spatial distribution of mass density of an object by acquiring 2D X-ray projections (each of them consisting of an X-ray radiography) that are then combined into a 3D image through the mathematical process known as reconstruction. Each X-ray radiography measures X-ray attenuation while X-rays propagate through the sample, with X-ray attenuation being a function of atomic number, density, and X-ray energy [10]. Depending on the energy of X-rays, the physical phenomenon mainly responsible for attenuation will be different: at low X-ray energy, photoelectric absorption is the main contributor to attenuation, whereas at high X-ray energy, Compton scattering (related to electron density) is the predominant effect [11]. Therefore, it is important to reach a sufficient X-ray energy level while scanning rocks saturated with fluids to ensure that X-ray attenuation, hence X-ray imaging, relies on substantial density and atomic number contrasts between the different phases present in the rock (solid and liquids). The 3D image of the sample is generated from the collection of 2D radiography images acquired at different angles through the process of image reconstruction. This computationally expensive mathematical process is the most crucial step for obtaining high-resolution 3D images; various algorithms can

be implemented, each with pros and cons, but all potentially affected by artifacts. Modern measurement techniques, however, help to remove these artifacts almost entirely. Despite the more common use of X-ray CT in the literature, especially in recent mud-filtrate invasion experimental research, some authors have preferred to reduce the scope of their studies to 2D X-ray radiography for a wide range of application. These includes visualization and characterization of multiphase flow [12, 13, 14], gravitational flow of particles [15], and monitoring of the frontal advance of fluids using gravity-led flow [16] or forced imbibition [17].

In our work, we chose to rely only on 2D radiography images, referred to as radiographs, to visualize the complexity/heterogeneity of each sample, and study and quantify mud-filtrate invasion in the pore space as well as mudcake deposition. This choice allows us to circumvent the reconstruction altogether, eliminating the need to correct for mathematical artifacts. Additionally, the flow cell no longer needs to be placed on a rotating stage during mud injection, eliminating challenges associated with the coupling of rotating and stationary elements. Nevertheless, the lack of reconstruction does not only bring about benefits: it also implies that we can only use 2D radiographs to quantify changes as a function of time in the rock sample as mud is being injected. Consequently, instead of using traditional, cylindrical cores, we employ thin rectangular-shaped rock samples. All experiments were carried out using 14 cm-long, 7 cm-wide, 0.6 cm-thick rock slabs. Because the thickness of each slab is one order of magnitude smaller than its width and length, the variability of rock properties perpendicular to the sample can be regarded negligible. For this reason, flow variability across the smallest dimension is considered negligible and the experiment becomes two-dimensional. In the case of laminated clastic rocks, some slabs were cut parallel to bedding planes while others were cut perpendicular to bedding planes, allowing us to study the effects of different heterogeneities on mud-filtrate invasion and mudcake deposition.

Table 1. Summary of petrophysical properties for the rock samples considered in this paper. Porosity was measured using the imbibition method. Permeability is brine permeability, while k_H and k_V refer to permeability parallel and perpendicular to laminations, respectively. The typical core used was approximately 1" in diameter and 5" long. Permeability was also measured using rock slabs. Each range was established using at least three data points.

Rock Core	Porosity	Permeability
ANTOLINI SANDSTONE laminated	11-14%	85-120 mD (k_H) 30-50 mD (k_V)
BEREA SANDSTONE	18-21%	25-80 mD
ESTAILLADES LIMESTONE	25-29%	110-190 mD
GRAY BERA	19-21%	74-78 mD
LEOPARD SANDSTONE	20-21%	160 – 300 mD
NUGGET SANDSTONE laminated	10-12%	55-65 mD (k_H) 0.5-1 mD (k_V)
SILURIAN DOLOMITE	16-17%	0.01-50 mD
UPPER GRAY BERA	20-22%	220-240 mD
“VUGGY” DOLOMITE	10-15%	0.04 mD-10 D

A wide range of rocks were examined for our study, ranging from homogeneous clastic rocks to complex carbonates with dual porosity. **Table 1** summarizes the rock samples used and their measured petrophysical properties. Slab permeability was measured using a probe permeameter. Each rock sample was dried at 100 °C for at least 24 hours prior to being embedded in the flow cell. Then, the sample was either used as is, for injection into air-saturated rocks, or saturated with either mineral oil or brine. The “vuggy” dolomite rock is a dolomite of unknown origin which exhibits zones of very low permeability and large vugs. Traditional, Hassler-type core holders are not suitable for this experimental procedure because they are typically made of stainless steel, a material that would interfere with X-ray attenuation. They are also designed for cylindrical cores in linear flow experiments. Instead, rock samples were embedded in rectangular flow cell made of polycarbonate, a material transparent to X-rays. High-strength epoxy was used to affix the slabs to their respective custom-made flow cells. **Figure 1** shows such a custom-made flow cell inside the microCT scanner cabinet. The flow cell is connected to the injection system that is also placed inside the shielded cabinet and controlled remotely.

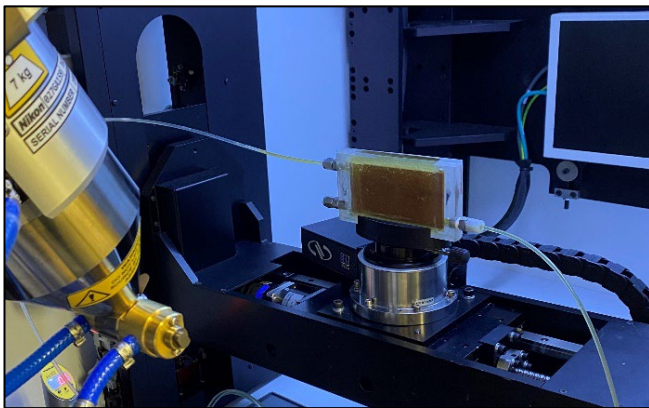


Fig. 1. Flow cell inside the microCT scanner cabinet. The custom-made flow cell is placed on the manipulator, between the X-ray gun (left) and the detector (back). The injection system is not visible on the photograph.

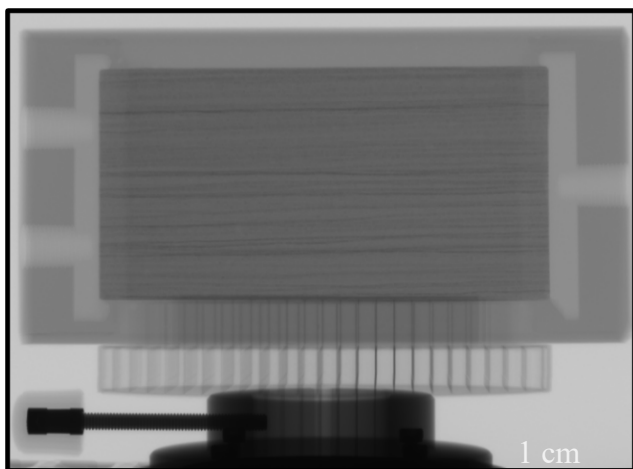


Fig. 2. X-ray radiography of a Nugget sandstone rock slab. The rock core is epoxied inside the polycarbonate frame that was designed for “two-dimensional” coreflood experiments.

Figure 2 shows an X-ray radiography of a Nugget sandstone rock slab epoxied into its plastic flow cell. On this radiograph, one can observe the rock slab itself, the polycarbonate frame (mostly transparent to X-rays, although the difference in plastic thickness is noticeable and the epoxy adds some material on top of the frame), the diffusers on both sides of the core (allowing each core to be used for two injection experiments), and the threaded ports (connections and tubing are not connected to the flow cell on this radiograph). On each end of the flow cell, inlet and outlet ports connect the tubing to diffusers, ensuring both a uniform flow on the surface of the slab and enough room for the mudcake to build up unrestrictedly. One can also observe the manipulator on which the flow cell is placed; the manipulator is used to position the rock sample perpendicularly to the incoming X-ray beam to satisfy the 2D assumption. When initiating an experiment, drilling mud is forced into the diffuser, the filter cake begins to form on the surface of the sample and mud filtrate, which cannot bypass the rock sample due to the epoxy, flows through the rock, invading the pore space. The flow is regarded to take place in the plane of the X-ray radiography.

Figure 3 shows a radiograph of two rock samples cut from the same block: one of the samples with bedding planes parallel to flow while the other exhibits bedding planes perpendicular to flow. By performing experiments with samples cut with laminations/bedding planes parallel and perpendicular to the pressure drop direction, it is possible to quantify the effects of rock anisotropy and heterogeneity on mud-filtrate invasion and mudcake buildup.



Fig. 3. X-ray radiographs of a laminated rock sample cut with bedding planes parallel (left panel) and perpendicular (right panel) to flow, respectively.

A Nikon XT-H 225 ST microCT scanner was used in this study, which includes a 225 kV microfocus source and a reflection target offering a 3 μm X-ray focal spot. Because the objective is to visualize flow at the core scale, and not at the pore scale, scan parameters were carefully selected such that acquisition time (i.e. time resolution) was optimized without affecting image resolution and/or noise. Depending on the rock sample being imaged, we achieved a resolution ranging from 17 to 50 μm. The typical scanning parameters responsible for this result are a beam energy of 110 kV, a beam current of 300 μA, and an exposure time of 708 ms. Copper filters of different thicknesses were employed to counterbalance image brightness resulting from the relatively high exposure time needed to attain acceptable resolution. X-ray radiographs are acquired quasi-continuously as drilling mud is being injected into the rock sample and mudcake is forming on the face of the core. Each pixel in a radiograph is assigned an X-ray attenuation number by the scanner, referred to as a grayscale number, which is related to the

average absorption coefficient of the different materials being imaged. As opposed to computed tomography, there is no automatic flux normalization available when using X-ray radiography. A correction factor is calculated based on grayscale fluctuations in pixels where no change is expected (such as the polycarbonate frame) and used to calibrate for variation of image brightness over time. This setting prevents offsets of grayscale number (due to flux oscillations) from producing non-physical values.

The experimental system, i.e. the X-ray gun, the detector, and the sample, is fully enclosed in a radiation shielding cabinet when the microCT scanner is energized, as per X-ray safety regulations. Therefore, a custom-made syringe pump is used to inject drilling mud into the rock samples; the pump is fully contained within the cabinet, is powered by batteries, and is operated remotely by a microcontroller connected via Bluetooth. Overbalance pressure, injection rate, and injected volume are the three quantities recorded and transmitted in real time to a computer during the experiment. The pressure is measured at the inlet with a high-accuracy pressure transducer. At the beginning of each experiment, drilling mud is injected into the sample by applying a pressure gradient; injection pressure is held constant by means of a proportional-integral-derivative control loop while the outlet is vented to ambient pressure.

Two drilling muds were used in this study: a water-base mud (WBM) and a synthetic oil-base mud (OBM). Both were characterized using API recommended practices; **Table 2** describes their measured properties. To secure an optimal contrast between the different fluid phases when the initial saturating fluid is not air, mineral oil and 30 wt% potassium iodide brine were used to initially saturate the samples with non-wetting and wetting phases, respectively.

Table 2. Summary of fluid properties for water-base mud (WBM) and synthetic oil-base mud (OBM).

Mud Properties	WBM	OBM
Mud specific gravity	1.3532	0.9334
Plastic Viscosity [cP]	24.4	18.9
Yield Point [lb _f /100 ft ²]	19	2.5
Gel Strength (10 sec.) [lb _f /100 ft ²]	2.9	1.8
Gel Strength (10 min.) [lb _f /100 ft ²]	4.3	2.3
API Loss @ 150°F [mL/30 min]	4.1	0.5
API Wet Cake Thickness [1/32 in.]	1.92	2.5
Solid Volume [%]	14	24
Water/Oil Ratio [v/v]	-	0.27

For each experiment, a baseline radiograph is acquired prior to starting the coreflood; at this point of the experiment, the sample is saturated with either a non-wetting phase (air or mineral oil) or a wetting phase (brine) depending on whether WBM or OBM is used, respectively. A second baseline radiograph is acquired after mud is injected to fill up the inlet diffuser, but before the system is pressurized. Baseline scans are used during data processing to make mud-filtrate invasion easily observable. MATLAB® was used to run the post-processing algorithm. Injection of drilling mud begins promptly after the acquisition of the baseline scans. A

pressure differential of 100 psi is applied to the sample by means of the syringe pump. This pressure differential, maintained constant throughout the experiment, induces mudcake formation on the face of the rock slab and mud-filtrate invasion inside the pore space of the sample.

Figure 4 illustrates both the baseline subtraction method and image processing technique with an Upper Gray Berea sample. The top left panel shows the raw radiograph of the baseline, air-saturated sample. One can observe the sample and the inlet diffuser on the left side of the image, filled with air. The radiograph shows a very homogeneous rock, as expected for an Upper Gray Berea. Any apparent heterogeneity is the result of the epoxy, not the sample (more visible on the bottom left panel). The top right panel shows the raw radiograph of the sample after 5.8 minutes of WBM injection at 100 psi overbalance pressure. One can already notice the mudcake deposition on the left face of the sample. It is also possible, albeit difficult, to distinguish a change in grayscale values inside the sample resulting from mud-filtrate invading the pore space and displacing air. The image in the bottom left panel is the heat, or color map of the top right panel, with a custom scale, making it easier to discern the invaded from the virgin zone. Finally, the bottom right panel shows the result of the baseline subtraction algorithm: the air-saturated radiograph (top left panel) is subtracted from the *in situ* scan acquired after 5.8 minutes of injection (top right panel).

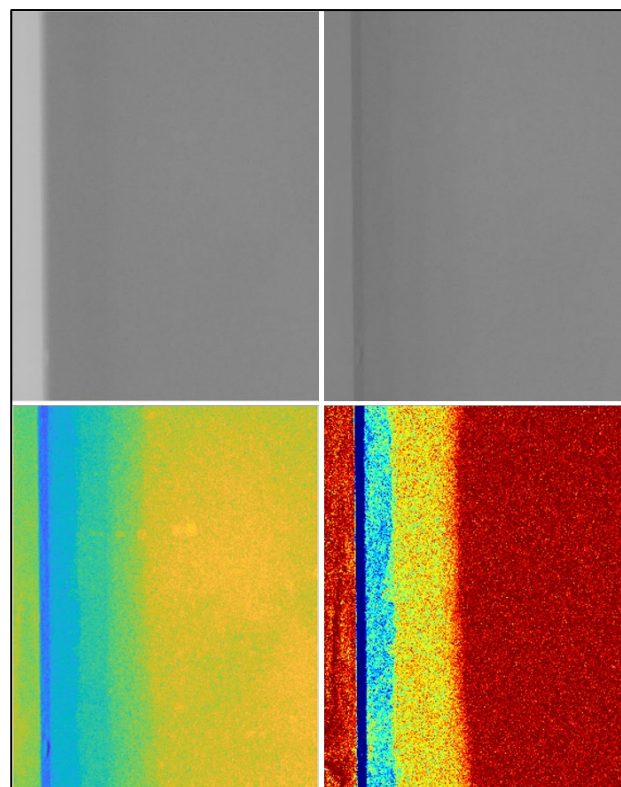


Fig. 4. Example of an WBM injection into an Upper Gray Berea sample illustrating the image processing method. Top left panel shows the baseline scan, acquired when the sample was air saturated. Top right panel shows the sample after 5.8 min of WBM injection at 100 psi overbalance. Bottom left panel shows the same scan with a different grayscale when loaded into MATLAB®. Bottom right picture shows the result of the baseline subtraction for the same time. The width of each image is 35 mm. No filter was applied to the images.

The red parts of the image correspond to zones where no change had occurred at this point in time during the experiment, while other colors, from yellow to dark blue, denote changes with respect to the initial state of the sample. As mudcake is being deposited on the face of the rock slab, the density of this area increases significantly, making it easy to determine its position and thickness. Mud-filtrate invasion inside the pores does not generate such a large density difference compared to the deposition of solid mud particles; therefore, changes with respect to the baseline radiograph are not as intense and shown in yellow in the processed image. This simple difference makes it easy to differentiate between mudcake and invaded zone. In this example, one notices that the invaded-zone color scale varies from yellow (as expected) to blue near the left face, a color that is supposed to indicate mudcake. This behavior is due to the geometry of the sample and how it is embedded in the plastic frame: at such early phase of the flow cell prototype, the rock slab protrudes from the epoxy coat and in the inlet diffuser in a way that makes 3 sides of it to be exposed to fluids in the diffuser (left face, as well as bottom and top face when looking at the image). Therefore, mudcake builds up not only on the left face of the sample, but also on the sides of the slab. However, the deposition is not unobstructed, as it is rapidly contacting the plastic frame, making the blue color on the image less deep than for mudcake building up on the left face of the rock slab. This instrumental drawback was fixed for subsequent cell flow prototypes, making sure that mudcake deposition occurred only on one face of the sample.

Because of the good resolution provided by this imaging method, the stacking of frames performed by the scanner to generate each radiograph (8 frames per image in this paper), and the natural good contrast between air and water-base mud filtrate, the locations of the invaded zone and mudcake are clearly visible in **Fig. 4**. Nevertheless, for other samples, determination of the precise location of the interface between virgin and invaded zones can be difficult because of the combined effects of random instrumental noise and small-scale heterogeneities; such effects are exacerbated by the image subtraction step. A 2D median filter was applied to each radiograph to circumvent the latter problem and improve the location of the invasion front while preserving edges when needed.

3 Results and discussion

This section describes several examples of drilling-mud injection experiments, starting from the simplest case, a homogeneous and isotropic Upper Gray Berea sandstone, to more complex rock samples such as heterogeneous and anisotropic clastic rocks, and highly heterogeneous carbonates. We also stress WBM injection experiments over OBM injection experiments, as the former is generally associated with deeper invasion and thicker mudcake, as expected from previously published studies [4, 18]. Likewise, we emphasize WBM invasion into air saturated samples, i.e., a connate fluid state seldom encountered in practice. The reason behind this choice was to simplify the proof of concept, as the density contrast between both types of drilling mud and air enables an easy observation of density variations within the flow cell (both inside the rock and in the diffuser).

As explained in the previous section, a 2D median filter was applied to every radiograph for all experiments; the filter is the same across all cases to facilitate image comparison. The spatial resolution and image length (i.e. in the direction of flow) are also consistent across all experiments described in this paper and equal to 29 microns and 35 millimeters, respectively. Drilling mud was injected at 100 psi overbalance for all experiments, and pump measurements (i.e. pressure, injected volume, and rate of injection) were recorded every 100 milliseconds.

Figure 5 shows the time-lapse mud-filtrate invasion and concurrent mudcake deposition of the same Upper Gray Berea experiment examined in the previous section. However, contrary to **Fig. 4**, a filter was applied in **Fig. 5**, making its effects on the data more conspicuous. The order of panels is from left to right, and top to bottom. Radiographs shown in **Fig. 5** were acquired after 0.5, 1, 3, 7, 32 and 75 min of WBM injection into the air-saturated sample. Upper Gray Berea is a very homogeneous, isotropic, and high permeability clastic rock; therefore, the observed front is almost vertical, and the displacement front is quasi piston-like, consistent with the Buckley-Leverett theory [19]. Such a behavior also explains why the invading front reaches the outer right edge of the image, indicating that the entire area displayed in the images has been invaded with drilling mud at approximately 75 minutes after the onset of the experiment. Nevertheless, one should note that the area displayed in **Fig. 5** does not correspond to the entirety of the sample: processed images were cropped to focus on the most relevant zones, and mud filtrate did not reach the other boundary of the rock slab.

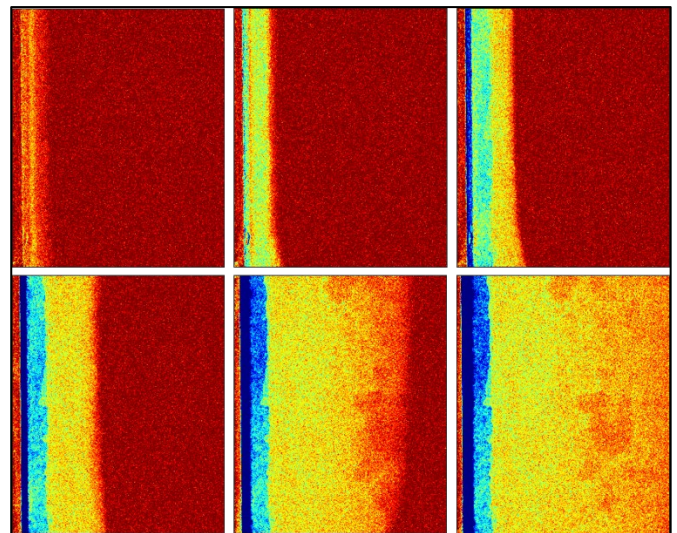


Fig. 5. WBM injection into an Upper Gray Berea sandstone sample. Each panel (from left to right and top to bottom) represents a radiograph acquired after 0.5, 1, 3, 7, 32 and 75 min of WBM injection into the air-saturated sample, respectively. The last radiograph was acquired at the time the saturation front reached the right edge of the image. Image width is 35 mm.

Figure 6 shows the mud-filtrate volume loss, i.e. invasion volume, as a function of time for both WBM and OBM injection into a Leopard sandstone core. The WBM injection experiment was carried out first on one side of the rock slab and, upon completion, OBM injection was initiated using the other side of the flow cell. The right panel shows the invasion volume in milliliters plotted against elapsed time in minutes,

while the left panel describes the same invasion volume, but plotted against the square-root of elapsed time. Plotting the mud-filtrate injected volume versus square-root of elapsed time is the standard approach to describing filtrate invasion data; obtaining a quasi-linear trend in the square-root of time domain is consistent with the filtration theory that governs the mud-filtrate invasion process [20]. The instantaneous volume of mud (filtrate and suspended particles) that flowed unobstructed at the beginning of both experiments before filter cake was formed, referred to as spurt loss, is visible on the left plot for both injections. This spurt effect is eliminated from the second plot by shifting the data in time before applying the square root.

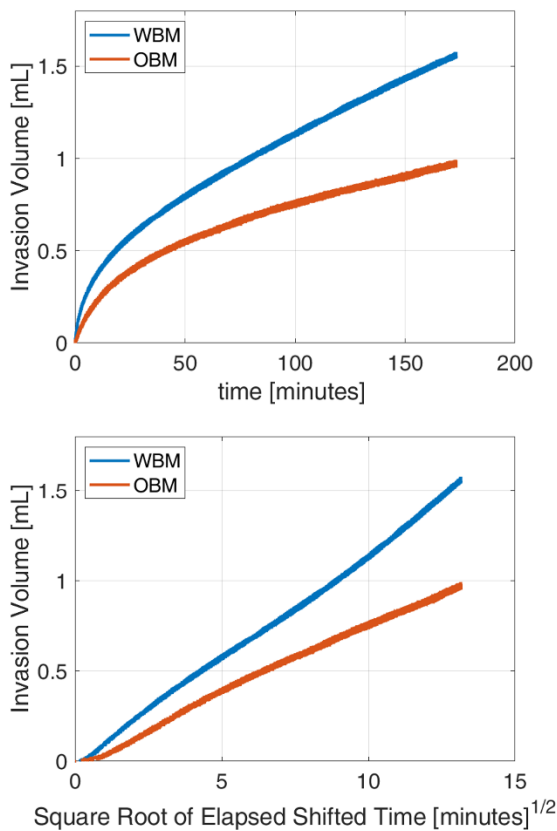


Fig. 6. Volume vs. time (top panel) and volume vs. square root of time (bottom panel) for an injection experiment into a Leopard sandstone sample using WBM and OBM.

As shown in **Fig. 6**, OBM injection is associated with a smaller cumulative mud-filtrate loss compared to WBM injection. However, the difference is not as large as expected, given previously reported results [4, 18], and field knowledge. The geometry of the sample might play an important role in this outcome and the geometrical factor should be investigated further.

Cases of application highlighted in this paper so far have been examples of homogeneous rocks. From this point onward, attention is switched to heterogeneous and anisotropic rocks, starting with a Nugget sandstone sample, i.e., a finely laminated clastic rock. **Figure 7** shows the time-lapse mud-filtrate invasion and concurrent mudcake deposition of the Nugget sandstone experiment. The sample was cut so that bedding planes were parallel to the flow direction. As opposed to **Fig. 5**, the first panel (top left) shows the radiograph of the dry sample in order to facilitate the

visual comparison of sample heterogeneity and the ensuing spatial distribution of fluids. The same format is adopted for all the subsequent figures. The next five panels shown in **Fig. 7** describe radiographs acquired after 1, 7, 14, 60 and 142 min of WBM injection into the air-saturated sample, respectively. Another notable difference with the previous example is the way in which the rock slab was embedded inside the plastic flow cell: instead of contacting different slab surfaces, the mud only contacts the left surface of the sample because of the slightly different design, making it impossible for mudcake to form anywhere else. The location of mudcake is therefore easier to determine compared to **Fig. 5**, and the 2D nature of the experiment is no longer affected by mudcake deposition outside of the plane of the sample. From the time-lapse radiographs, we observe that the evolution of the invasion front is not piston-like anymore and remains highly influenced by the thin laminations present in the sample. Despite some crossflow occurring during injection, the invasion front becomes more and more irregular as additional mud is injected into the sample, while the thickness of the mudcake is not constant along the direction perpendicular to flow.

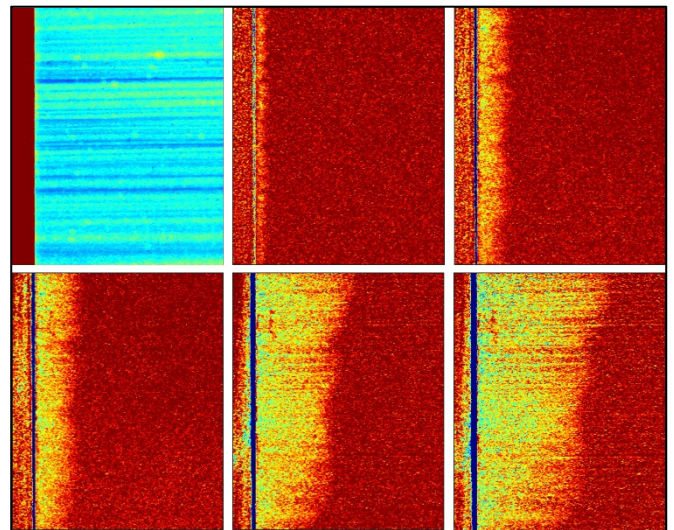


Fig. 7. WBM injection into a Nugget sandstone sample. The first (top left) panel is a grayscale map (with enhanced colors) of the sample, showcasing the heterogeneity of the rock sample. Each subsequent panel (from left to right and top to bottom) represents a radiograph acquired after 1, 7, 14, 60 and 142 min of WBM injection into the air-saturated sample, respectively. Image width is 35 mm.

Figure 8 shows the time-lapse mud-filtrate invasion and concurrent mudcake deposition for an Antolini sandstone experiment. In this experiment, the rock slab was also cut such that the laminations were parallel to the flow direction. As mentioned above, the first panel shows the grayscale map of the sample. Notice from the grayscale map that the round feature present is not a rock feature, but an air bubble trapped in epoxy. This situation does not affect the baseline subtraction results, as the bubble is present in every radiograph and is subtracted out in the process. The next five panels show time-lapse radiographs acquired after 1, 6, 16, 27 and 62 min of WBM injection into the air-saturated sample, respectively. Even when the Nugget and the Antolini sandstones can both be described as laminated clastic rocks the thickness of their laminations is different. Contrary to the

previous example that featured a thinly laminated Nugget sandstone, the Antolini sandstone exhibits thicker layers, each consisting of different petrophysical properties, while crossflow only takes place at the edges of these layers. One can notice that the unevenness of the invasion front at early times of injection is progressively leveled out, thanks to both crossflow and the smaller sample anisotropy compared to the Nugget sandstone. This observation correlates well with the information of **Table 1**, which indicates that the permeability of Antolini sandstone perpendicular to laminations (i.e. the “perpendicular” permeability) is only half the value of the “parallel” permeability, whereas the “perpendicular” permeability of the Nugget sandstone is one order of magnitude smaller than its “parallel” permeability. Finally, one can readily correlate the higher permeability streaks with the thickness of mudcake.

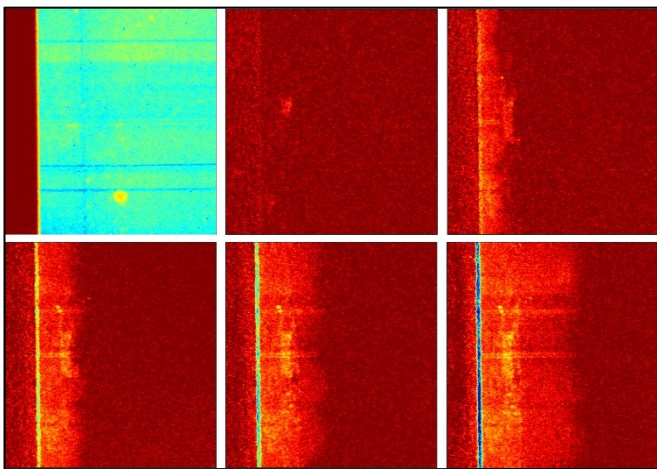


Fig. 8. WBM injection into a Antolini sandstone sample, with laminations parallel to the flow direction. The first panel is a grayscale map (with enhanced colors) of the sample, showcasing the heterogeneity of the rock sample. Each subsequent panel (from left to right and top to bottom) represents a radiograph acquired after 1, 6, 16, 27 and 62 min of WBM injection into the air-saturated sample, respectively. Image width is 35 mm.

Figure 9 shows the time-lapse mud-filtrate invasion and concurrent mudcake deposition for an Antolini sandstone experiment. In this experiment, the rock slab was cut such that the laminations were perpendicular to flow, and the rock sample was cored out of the same block as the sample described in **Fig. 8**. Once again, the first panel shows the grayscale map of the sample while the next five panels correspond to time-lapse radiographs acquired after 1, 6, 20, 97 and 300 min of WBM injection into the air-saturated sample, respectively. As expected, given the constant overbalance pressure applied to the sample for all experiments, it takes a longer injection time to reach approximately the same length of invasion compared to the previous example, due to the lower permeability of the sample with laminations perpendicular to the flow direction. The invasion front is also expected to be more uniform and approaching a piston-like displacement. However, such is not the case for this example, as mud filtrate bypasses low-permeability layers because the latter layers are not continuous across the sample. This behavior takes place in areas of the rock sample that are outside the zone of interest shown in the images. It becomes conspicuous in the last two

panels, showing changes with respect to the baseline scan ahead of the main front (a behavior also well represented in the last two cases examined in this paper, showcasing carbonate rocks). Apart from this observation, mudcake deposition is very uniform in **Fig. 9**.

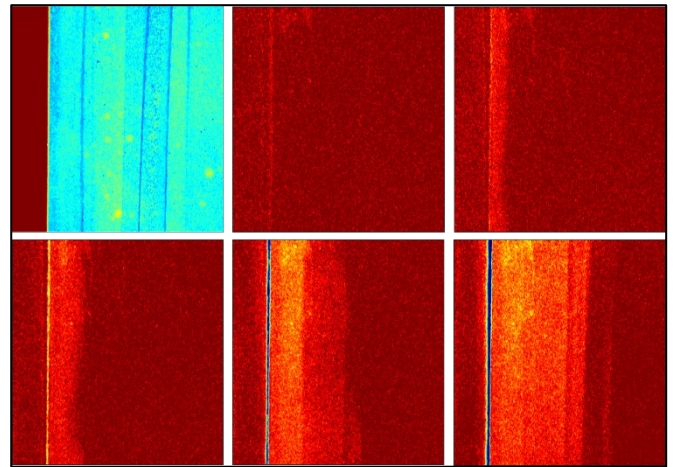


Fig. 9. WBM injection into a Antolini sandstone sample, with laminations perpendicular to the flow direction. The first panel is a grayscale map (with enhanced colors) of the sample, showcasing the heterogeneity of the rock sample. Each subsequent panel (from left to right and top to bottom) represents a radiograph acquired after 1, 6, 20, 97 and 300 min of WBM injection into the air-saturated sample, respectively. Image width is 35 mm.

Figure 10 shows the time-lapse mud-filtrate invasion and concurrent mudcake deposition for a “Vuggy” dolomite sample. The sample is of unknown origin and exhibits relatively large vugs, spanning from a few millimeters to the centimeter scale. The top left panel shows the grayscale map of the sample, where the vug structure is highlighted.

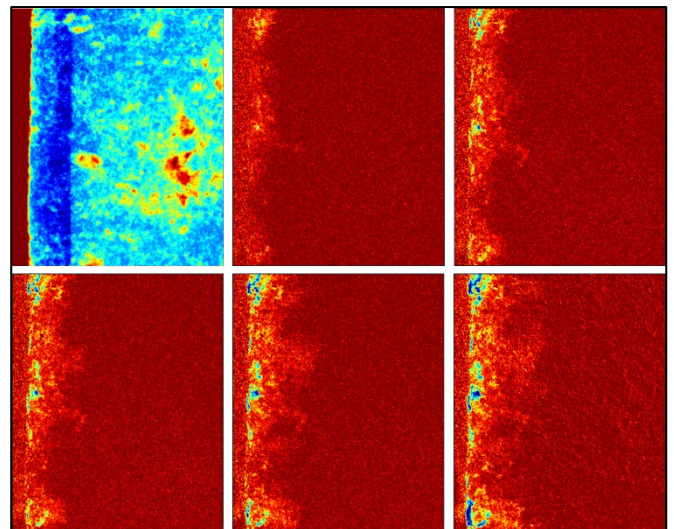


Fig. 10. WBM injection into a “Vuggy” Dolomite sample. The first panel is a grayscale map (with enhanced colors) showcasing the heterogeneity of the rock sample. Each subsequent panel (from left to right and top to bottom) represents a radiograph acquired after 1, 5, 8, 16 and 72 min of WBM injection into the air-saturated sample, respectively. Image width is 35 mm.

It should be noted that, because of the way the sample was epoxied inside the plastic frame, some vugs might be filled with resin, making them impermeable to any fluid. It is

difficult to assess beforehand the effect of epoxy on the sample, especially in vuggy carbonates. However, by monitoring the change in density with respect to the baseline and recording the volume injected as a function of time, we are able to describe fluid flow in vuggy carbonates as shown in this example and the next one. The next five panels of **Fig. 10** show time-lapse radiographs acquired after 1, 5, 8, 16 and 72 min of WBM injection into the air-saturated sample, respectively. As expected for a carbonate sample, some parts of the core are virtually impermeable to flow at this pressure, and mudcake cannot be deposited uniformly on the face of the slab. Mudcake deposition and mud-filtrate invasion occur only within segments of the sample that are permeable, i.e., in vugs. Contrary to previous examples, internal mudcake deposition is evident in this case. External mudcake is also discontinuous and the depth of invasion is significantly smaller than in clastic rocks. This behavior is attributed to the fact that existing pores are not well connected, and mud filtrate must fill internal vugs before invading the next section of the sample. Finally, the change of density with respect to the baseline scan is smaller compared to previous cases, hence the darker, reddish tinge of the “area of invasion”, compared to the more yellowish ones present in clastic rock samples.

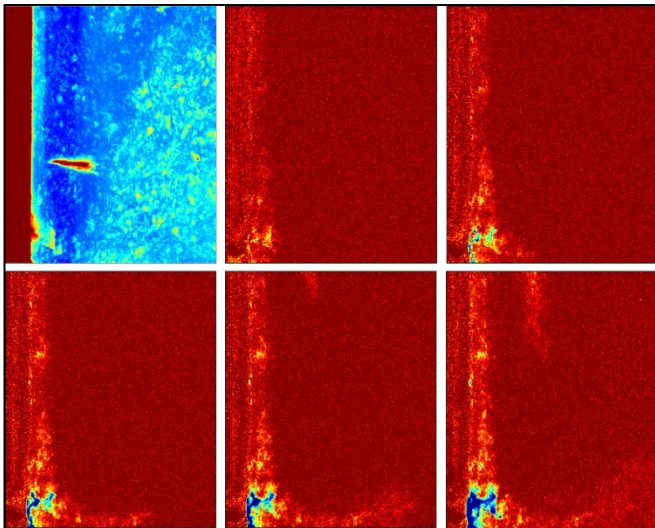


Fig. 11. WBM injection into a Silurian Dolomite sample. The first panel is a grayscale map (with enhanced colors) showcasing the heterogeneity of the rock sample. Each subsequent panel (from left to right and top to bottom) represents a radiograph acquired after 1, 5, 8, 17 and 68 min of WBM injection into the air-saturated sample, respectively. Image width is 35 mm.

Figure 11 describes the time-lapse mud-filtrate invasion and concurrent mudcake deposition for a Silurian dolomite experiment. This carbonate sample also exhibits vugs, but in a smaller extent compared to the previous case. Once again, the top left panel shows the grayscale map of the sample, where the vug system is visible. The next five panels of **Fig. 11** show time-lapse radiographs acquired after 1, 5, 8, 17 and 68 min of WBM injection into the air-saturated sample, respectively. Very similarly to the “Vuggy” dolomite sample, most of the mud-filtrate invasion and mudcake deposition take place where vugs are present. However, contrary to the previous example, most of the borehole face is impermeable and the vast majority of the invasion processes, including the

formation of external and internal mudcake, take place at the bottom of the image, where a substantial vug is present. Nevertheless, it can be noticed that some mud-filtrate invasion occurs at late times at the top of the radiographs too, following a permeable streak present in the rock. This behavior originates from the presence of a very similar vug located just above the window of interest displayed in **Fig. 11**, allowing for mudcake formation and mud-filtrate invasion to take place.

4 Summary and conclusions

We developed and verified a new high-resolution imaging technique to evaluate mud-filtrate invasion and mudcake deposition using “two-dimensional” injection experiments and X-ray radiography. The relevance of the experimental method was tested using a wide range of rock samples, from homogeneous clastic rocks to spatially complex carbonates exhibiting dual porosity. Injection experiments were performed using rectangular rock samples, an automated drilling mud injection system, and a microCT scanner. Water- and oil-base drilling muds were injected using a custom-made polycarbonate flow cell at a constant inlet pressure while the cores were quasi-continuously scanned using high-resolution X-ray radiography. Because rock slabs have a width one order of magnitude smaller than the remaining two dimensions, all invasion processes are regarded as two-dimensional and only X-ray radiographs are used to monitor them. By using reference radiographs acquired before mud pressurization, mud-filtrate invasion and mudcake deposition on the borehole wall were examined as a function of time and the effects of different rock heterogeneities on mud-filtrate invasion and mudcake formation were examined in detail.

Experimental results confirmed that 2D imaging using a microCT scanner enables the *in situ* visualization of the space-time distributions of (1) mud filtrate and (2) external and internal mudcake deposition, as already described for coreflood experiments of immiscible fluids in Aérens et al. [21]. Estimation of the time-lapse precise position and, more importantly, shape of the interface between the virgin zone and the mud-filtrate invaded zone is one, if not the most crucial contribution of this experimental method, along with the *in situ* measurement of mudcake buildup. Contrary to two-phase coreflood experiments, it is not possible to reach a state where the pore space has been mostly swept by mud filtrate (i.e., saturation of connate fluids approaches residual saturation), due to the very low permeability of mudcake and, therefore, the very low associated flow rate. This behavior means that explicit saturations cannot be directly calculated from the radiographs. However, the interface between mud filtrate and saturating fluids, and the 2D area corresponding to the invaded zone are both measurable physical quantities. Results are consistent with the theory of mud-filtrate invasion into porous rocks: injection of WBM results in longer mudcake deposition period, thicker mudcake, and higher filtrate invasion volume when compared to OBM. Our method yields a spatial resolution up to one order of magnitude higher than methods involving traditional medical X-ray scanners (conventional medical CT scanners have a resolution of 0.5 to 1 mm for decimeter-scale samples while micro-focus scanners have a resolution of approximately a

few tens of microns for centimeter-scale samples) and enables a better time resolution than with computed tomography experiments. Finally, data processing for this new method is also faster than with traditional CT scanners due to the lack of an image reconstruction step.

Furthermore, our experimental data unveil the strong correlation between the spatial distribution of mud filtrate (and mudcake deposition) and rock heterogeneity. Results indicate that spatial heterogeneity and anisotropy in both clastic and carbonate rocks remarkably influence the spatial distribution of fluids in the pore space and indicate that rock transmissibility has a significant impact on fluid-saturation distribution at high injection volumes. At early times of injection, mud filtrate preferentially follows higher permeability/porosity layers or veins. However, heterogeneous fluid distributions become homogenized as additional mud is injected when vertical transmissibility is significant, i.e., mainly in clastic laminated rocks. In the case of vuggy carbonates, lack of vertical transmissibility prevents this homogenization process to take place, leading to very “patchy” spatial distributions of filtrate, even at late times of injection. The latter observation has important consequences in the interpretation of borehole geophysical measurements is affected by the spatial distribution of fluids around the wellbore. More notably, results provide guidance to estimate fluid saturation from resistivity measurements acquired in spatially complex rocks.

Finally, our results show noteworthy differences in the invasion process whether water-based or oil-base mud is employed during drilling; differences are observed for mud-filtrate invasion in the pore space itself but also during mudcake deposition on the borehole wall. Results agree with field and previously reported laboratory observations: mudcake thickness and mud-filtrate volume loss are consistently higher in WBM experiments compared to OBM experiments. The peculiar geometry of the rock samples examined in this paper also enables the study of the effect of anisotropy on invasion processes by cutting rock slabs parallel and perpendicular to laminations. Overall, our method is fast and reliable to assess the influence of rock heterogeneity, anisotropy, and more generally, rock and fluid properties on mud-filtrate invasion and mudcake deposition.

We restate that the work reported in this paper emphasized WBM injection into air-saturated samples to streamline the validation and verification of the experimental methods. Future work includes performing additional experiments on spatially complex rocks to scrutinize the effect of different connate fluids on the final state of the rock sample and increasing overbalance pressures to bring this experimental procedure closer to field conditions.

Acknowledgements

The work reported in this paper was funded by The University of Texas at Austin’s Research Consortium on Formation Evaluation, jointly sponsored by Anadarko, Aramco, Baker Hughes, BHP, BP, Chevron, China Oilfield Services Limited, CNOOC International, ConocoPhillips, DEA, Eni, Equinor ASA, ExxonMobil, Halliburton, INPEX, Lundin Norway, Occidental, Oil Search, Petrobras, Repsol, Schlumberger, Shell, Southwestern, Total, Wintershall Dea, and Woodside Petroleum Limited.

X-ray scanning was performed at the Chevron Digital Petrophysics Laboratory (Hildebrand Department of Petroleum and Geosystems Engineering at The University of Texas at Austin).

List of Acronyms

CT	Computed Tomography
microCT	microfocus computed tomography
2D	two-dimensional
3D	three-dimensional
WBM	water-base mud
OBM	synthetic oil-base mud
MICP	Mercury Intrusion Capillary Pressure
NMR	Nuclear Magnetic Resonance

References

1. B. Voss, C. Torres-Verdín, A. Gandhi, G. Alabi, M. Lemkecher. *Common stratigraphic framework to simulate well logs and to cross-validate static and dynamic petrophysical interpretations*. Paper presented at the 50th SPWLA Symposium. (2009)
2. P. Jones, E. Babson, *Evaluation of rotary-drilling muds*, Drilling and Production Practice, pp. 22-33. (1935)
3. M. Chenevert, J Dewan. *A model for filtration of water-base mud during drilling: determination of mudcake parameters*. *Petrophysics*, **42**(03): 237-250. (2001)
4. C. Schroeder, C. Torres-Verdín. *Experimental Method for Time-Lapse Micro-CT Imaging of Mud-Filtrate Invasion and Mudcake Deposition*. *Petrophysics*, **60**(05): 620-630. <https://doi.org/10.30632/PJV60N5-2019a6>. (2019)
5. M. Honarpour, F. Koederitz, A. Herbert. *Relative Permeability of Petroleum Reservoirs*. Boca Raton, Florida: CRC Press. (1986)
6. S. Wellington, H. Vinegar. *X-Ray Computerized Tomography*. *J. Pet. Technol.*, **39**(08): 885–898. <https://doi.org/10.2118/16983-PA>. (1987)
7. R. Ketcham, W. Carlson. *Acquisition, Optimization and Interpretation of X-Ray Computed Tomographic Imagery: Applications to the Geosciences*. *Comp. & Geosc.*, **27**(04): 381-400. [https://doi.org/10.1016/S0098-3004\(00\)00116-3](https://doi.org/10.1016/S0098-3004(00)00116-3). (2001)
8. D. Wildenschild, A. Sheppard. *X-Ray Imaging and Analysis Techniques for Quantifying Pore-Scale Structure and Processes in Subsurface Porous Medium Systems*. *Advances in Water Resources*, **51**: 217-246. <https://doi.org/10.1016/j.advwatres.2012.07.018>. (2013)
9. J. Luo, D. Espinoza, Q. Nguyen. *X-Ray Micro-Focus Monitoring of Water Alternating Gas Injection in Heterogeneous Formations*. Paper presented at the SPE Impr. Oil Recov. Conference. <https://doi.org/10.2118/190223-MS>. (2018)
10. R. Ketcham, G. Iturrino, *Nondestructive High-Resolution Visualization and Measurement of Anisotropic Effective Porosity in Complex Lithologies Using High-Resolution X-Ray Computed Tomography*.

- Journal of Hydrology, **302**(1-4): 92-106. (2005).
<https://doi.org/10.1016/j.jhydrol.2004.06.037>.
11. J. Hsieh, *Computed Tomography: Principles, Design, Artifacts, and Recent Advances*. Bellingham, Washington: SPIE Press (2003)
 12. T. Heindel, J. Gray, T. Jensen, *An X-ray System for Visualizing Fluid Flows*. Flow Meas. Instr., **19**(2): 67–78.<http://dx.doi.org/10.1016/i.flowmeasinst.2007.09.003>.(2008)
 13. T. Heindel, *A Review of X-Ray Flow Visualization with Applications to Multiphase Flows*. J. Fl. Eng., **133**(7): 074001. <https://doi.org/10.1115/1.4004367>. (2011)
 14. A. Skauge, P. Ormehaug, T. Gurholt, B. Vik, I. Bondino, I., G. Hamon. *2-D Visualisation of Unstable Waterflood and Polymer Flood for Displacement of Heavy Oil*. Paper presented at the SPE Improved Oil Recovery Symposium. <https://doi.org/10.2118/154292-MS>. (2012)
 15. A. Romanowski, P. Luczak, K. Grudzien, *X-ray Imaging Analysis of Silo Flow Parameters Based on Trace Particles Using Targeted Crowdsourcing*. Sensors, **19**(15): 3317. <http://dx.doi.org/10.3390/s19153317>. (2019)
 16. V. Cnudde, M. Dierick, J. Vlassenbroeck, B. Masschaele, E. Lehmann, P. Jacobs, L. Van Hoorebeke. *High-speed Neutron Radiography for Monitoring the Water Absorption by Capillarity in Porous Materials*. Nuclear Instruments & Methods in Physics, **266**(1):155–163.<https://doi.org/10.1016/j.nimb.2007.10.030>. (2008)
 17. M. Zambrano, F. Hammed, K. Anders, L. Mancini, E. Tondi. *Implementation of Dynamic Neutron Radiography and Integrated X-Ray and Neutron Tomography in Porous Carbonate Reservoir Rocks*. Frontiers in Earth Science, **7**:329.<https://doi.org/10.3389/feart.2019.00329>. (2019)
 18. C. Schroeder, C. Torres-Verdín. *In-Situ Visualization and Characterization of Filter-Cake Deposition Using Time-Lapse Micro-CT Imaging*. Petrophysics, **63**(02): 199-217. <https://doi.org/10.30632/PJV63N2-2022a4>. (2022)
 19. S. Buckley, M. Leverett. *Mechanism of Fluid Displacement in Sands*. Trans. of the SPE, **146**, Part I, 107-116. <https://doi.org/10.2118/942107-G>. (1942)
 20. W. Chin. *Formation Invasion: With Applications to Measurement-While-Drilling, Time-Lapse Analysis, and Formation Damage*. Gulf Professional Publishing. (1995)
 21. P. Aérens, C. Torres- Verdín, N. Espinoza. *Experimental Investigation of Two-Phase Flow Properties of Heterogeneous Rocks for Advanced Formation Evaluation*. Paper presented at the SPE ATCE conference <https://doi.org/10.2118/206334-MS>. (2021)